FOSSEE, IIT Bombay
OpenFOAM Case Study Project
December 18, 2025

Exploring Overset Meshes for Moving Body Problems Using OpenFOAM

Bhadri Srivatshan K. R.[1], Parees Palkar[2], Chandan Bose[3]

[1]Department of Aerospace Engineering, Amrita Vishwa Vidyapeetham
[2]FOSSEE, Indian Institute of Technology Bombay
[3]Assistant Professor, Aerospace Engineering, College of Engineering and Physical Sciences, University of Birmingham, UK

ABSTRACT

The free fall of rigid bodies in a fluid exhibits a wide range of unsteady motion regimes due to strong coupling between rigid-body dynamics and wake-induced flow structures. In the present work, an overset-mesh-based numerical framework is developed in OpenFOAM to simulate a freely falling rigid body undergoing large translational and rotational motion. Independent background and body-fitted meshes are generated and coupled through overset interpolation, enabling stable mesh motion without deformation. Detailed simulations of a flat plate with finite thickness are performed over a range of density ratios. The resulting descent dynamics, including steady fall, flutter, and strongly inertial oscillatory regimes, are shown to be in qualitative agreement with established experimental and numerical studies.

Contents

List of Figures

List of Tables

OpenFOAM Case Study Project
FOSSEE, IIT Bombay

1 Introduction

The free fall of rigid plates in a fluid exhibits a range of unsteady motion patterns, including steady descent, fluttering oscillations, and tumbling or autorotational motion. These behaviors arise from the strong coupling between rigid-body dynamics and unsteady flow structures in the wake. Despite the geometric simplicity of the system, freely falling plates represent a widely studied benchmark problem in fluid–structure interaction and unsteady aerodynamics, and have been extensively studied as a model system for understanding vortex-induced forces and coupled translational–rotational dynamics.

Previous experimental and numerical investigations have shown that the falling behavior of plates is governed primarily by a small set of non-dimensional parameters, including the Reynolds number, thickness-to-length ratio, and density ratio, and the dimensionless moment of inertia. For plates with relatively low inertia, angular perturbations decay and the body approaches a steady vertical descent. As inertia increases, the steady state loses stability and is sustained fluttering oscillations develop, which may further transition to continuous tumbling motion depending on the plate geometry and mass distribution [1, 2]. The role of density ratio and plate thickness in promoting or suppressing flutter has been examined in detail in both numerical and experimental studies, with heavier and thicker plates tending to exhibit inertia-dominated dynamics such as tumbling or strongly damped oscillations [3, 4].

Reduced-order models based on inviscid vortex-sheet formulations have been successful in reproducing the qualitative features of fluttering and tumbling motions over a range of parameters, offering valuable physical insight into the underlying mechanisms [1, 5]. However, resolving the near-body flow, viscous effects, and wake development for plates with finite thickness requires direct numerical solution of the Navier–Stokes equations. Such simulations are computationally challenging due to the large-amplitude motion of the body and the need to accurately couple the fluid forces with the rigid-body response.

In this work, an overset-mesh-based computational framework is employed to simulate the free fall of rigid bodies undergoing large translations and rotations. Overset meshes allow independent generation of stationary background grids and body-fitted moving grids, making them well-suited for problems involving large rigid-body motion without mesh distortion. The numerical approach is implemented in OpenFOAM using a two-dimensional, laminar flow formulation fully coupled with rigid-body dynamics.

The focus of the study is the free fall of a flat plate with a finite thickness-to-length ratio of 0.1, examined over density ratios ranging from $\rho^* = 8.5$ to 100. This range spans steady descent, fluttering, and strongly inertial regimes reported in the literature. The objective of the present case study is not to introduce new physical models, but to document a clear and reproducible

overset-mesh simulation procedure and to examine the resulting qualitative descent dynamics in relation to established experimental and numerical findings. .

2 Governing Equations

The flow is modeled as an incompressible, Newtonian fluid fully coupled with the motion of a rigid body. A two-dimensional formulation is adopted, which is appropriate for freely falling plates with sufficiently large span-to-chord ratios, where out-of-plane effects can be neglected [1, 2].

2.1 Fluid and Rigid-Body Equations

The fluid motion is governed by the incompressible Navier–Stokes equations,

$$\nabla \cdot \mathbf{u} = 0, \tag{1}$$

$$\frac{\partial \mathbf{u}}{\partial t} + \nabla \cdot (\mathbf{u}\mathbf{u}) = -\frac{1}{\rho_f}\nabla p + \nu \nabla^2 \mathbf{u} + \mathbf{g}, \tag{2}$$

where **u** is the velocity vector, p is the kinematic pressure, ρ_f is the fluid density, ν is the kinematic viscosity, and **g** represents gravitational acceleration.
The rigid body motion is described by the Newton–Euler equations for translation and rotation,

$$m\frac{d^2\mathbf{x}}{dt^2} = \sum \mathbf{F}, \tag{3}$$

$$I\frac{d^2\theta}{dt^2} = \sum M, \tag{4}$$

where m and I denote the mass and moment of inertia of the body, **x** is the position of the center of mass, and θ is the angular orientation about the out-of-plane axis.
The hydrodynamic forces **F** and moments M acting on the body are obtained by integrating pressure and viscous stresses over the body surface at each time step. These forces are passed to the rigid-body motion solver, and the resulting translational and rotational velocities are used to update the body motion in a fully coupled manner.

2.2 Non-Dimensional Parameters

The descent dynamics are characterized using non-dimensional parameters derived from the geometric and inertial properties of the plate. Following previous studies [1, 2, 3], the dimensionless moment of inertia is defined as

$$I^* = \frac{I}{I_d} = \frac{8\rho_s h(L^2 + h^2)}{3\pi\rho_f L^3}, \tag{5}$$

where ρ_s and ρ_f are the solid and fluid densities, L is the plate length, and h is the plate thickness. The density ratio and thickness ratio are defined as

$$\rho^* = \frac{\rho_s}{\rho_f}, \qquad \beta = \frac{h}{L}. \tag{6}$$

An inertia-based Froude number, defined using the terminal velocity (U_T), is also introduced as [5]

$$Fr = \frac{U_T^2}{gL} = \frac{\rho_s - \rho_f}{\rho_f}\frac{h}{L}, \tag{7}$$

which scales proportionally with the dimensionless moment of inertia and provides an alternative measure of inertial dominance.

2.3 Modeling Assumptions

All simulations are performed under the assumption of two-dimensional laminar flow. The Reynolds numbers associated with the descent remain within a range where large-scale unsteady vortex shedding dominates, and no turbulence modeling is employed. The body is assumed to be perfectly rigid with finite thickness, and fluid-structure coupling is fully resolved through instantaneous force and moment exchange. Density ratios between 8.5 and 100 are considered, covering inertia-dominated regimes reported in the literature [3, 4].

3 Overset Mesh Methodology

Overset mesh methodology is employed to simulate large rigid-body motions without mesh deformation. The approach uses independently generated background and moving meshes, coupled through interpolation, and is well-suited for freely falling bodies.

3.1 Case Organization

The computational setup consists of a stationary background mesh representing the far-field domain and a moving overset mesh enclosing the rigid body. Both meshes are generated independently using `blockMesh` and combined using `mergeMeshes`, allowing independent refinement and robust handling of large motions.

3.2 Overset Region Identification

After merging, overset regions are identified using `topoSet` based on mesh regions. Cells belonging to the overset mesh are selected using the `regionToCell` source by specifying a point inside the overset region, while background cells are obtained by inversion. Hole cutting is han-

dled internally by the overset algorithm during the simulation through fringe cell identification and interpolation.

3.3 Zone Identification and Interpolation

Zone identifiers are assigned using `setFields`, with `zoneID = 0` for overset cells and `zoneID = 1` for background cells. Overset interpolation is controlled in `fvSchemes` using the `oversetInterpolation` dictionary, where interpolation method and stencil parameters are specified to ensure stable coupling.

3.4 Rigid-Body Motion and Boundary Conditions

Rigid-body motion is prescribed through `dynamicMeshDict` using `dynamicOversetFvMesh` coupled with a six-degree-of-freedom motion solver. Physical properties, gravity, and time integration schemes are defined here. Overset interfaces use the `overset` boundary type, while standard wall and far-field boundary conditions are applied elsewhere.

3.5 Summary

The overset mesh framework enables the stable simulation of freely falling rigid bodies by combining independent mesh generation, region-based overset classification, controlled interpolation, and fully coupled rigid-body motion. This methodology forms the numerical basis for the simulations presented in the following section.

4 Simulation Procedure

Using the overset mesh framework described in the previous section, numerical simulations are carried out for a freely falling rigid body. The simulation setup is summarized below through geometry description, mesh configuration, boundary patches, initial and boundary conditions, and solver parameters. All simulations are performed using `OpenFOAM` version 2506.

4.1 Geometry Overview

All simulations are performed in a two-dimensional framework with unit depth assumed in the out-of-plane direction. A flat plate is considered as the geometry of interest.

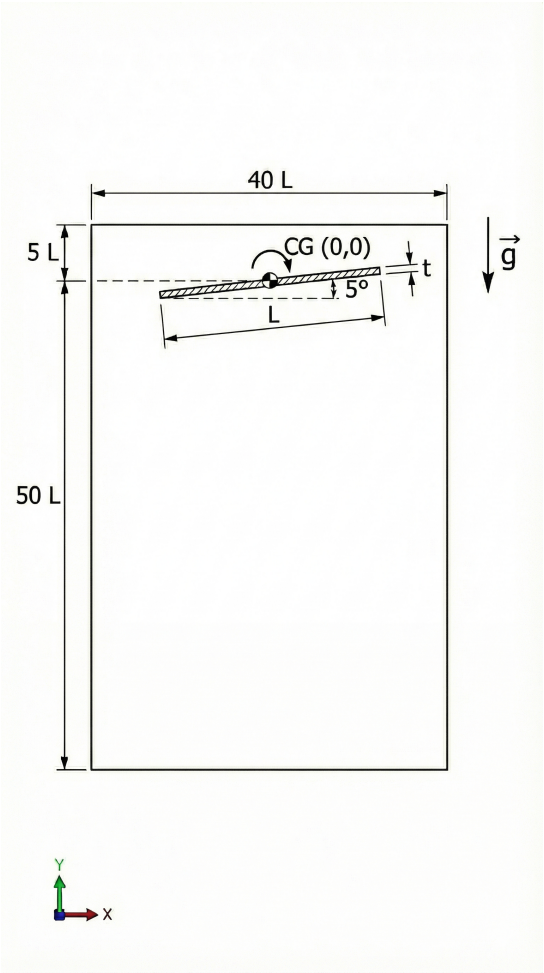

Figure 1: Computational domain and initial configuration of the freely falling flat plate considered in the present study. The background domain and initial body placement are shown in a two-dimensional framework.

Table 1: Geometric parameters of the simulated flat plate

Parameter	Value
Length, L (m)	1.0
Thickness, h (m)	0.1
Thickness ratio, h/L	0.1
Degrees of freedom	Translation + Rotation

4.2 Computational Domain and Mesh

A structured background mesh and a body-fitted overset mesh are generated independently using `blockMesh`. The background mesh represents the far-field domain, while the overset mesh encloses the rigid body and moves with it during the simulation.

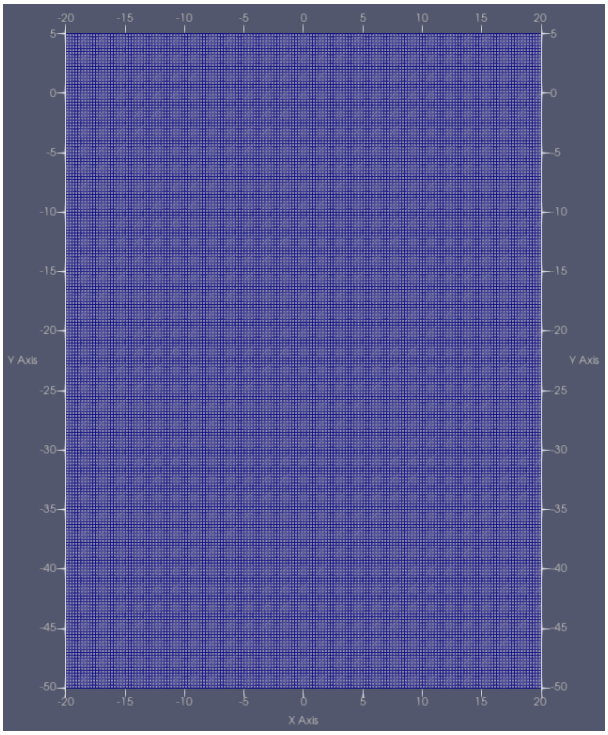

Figure 2: Structured background computational domain and mesh used to represent the far-field region. The domain is sufficiently large to minimize boundary effects on the motion of the freely falling body.

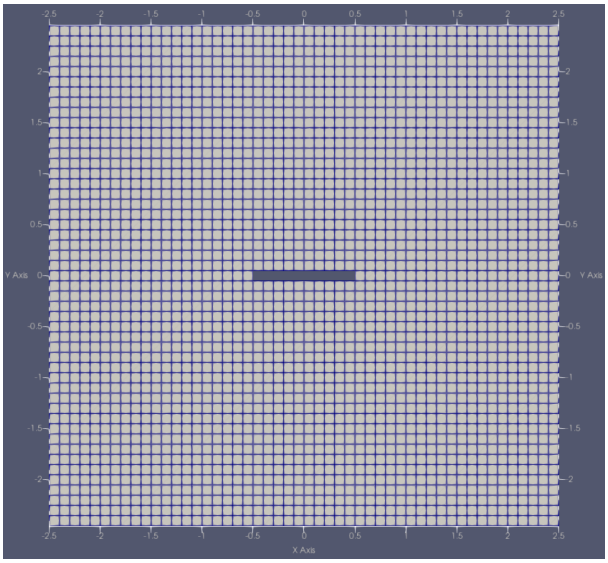

Figure 3: Body-fitted overset mesh enclosing the flat plate prior to mesh merging. The locally refined structured grid moves with the rigid body during the simulation.

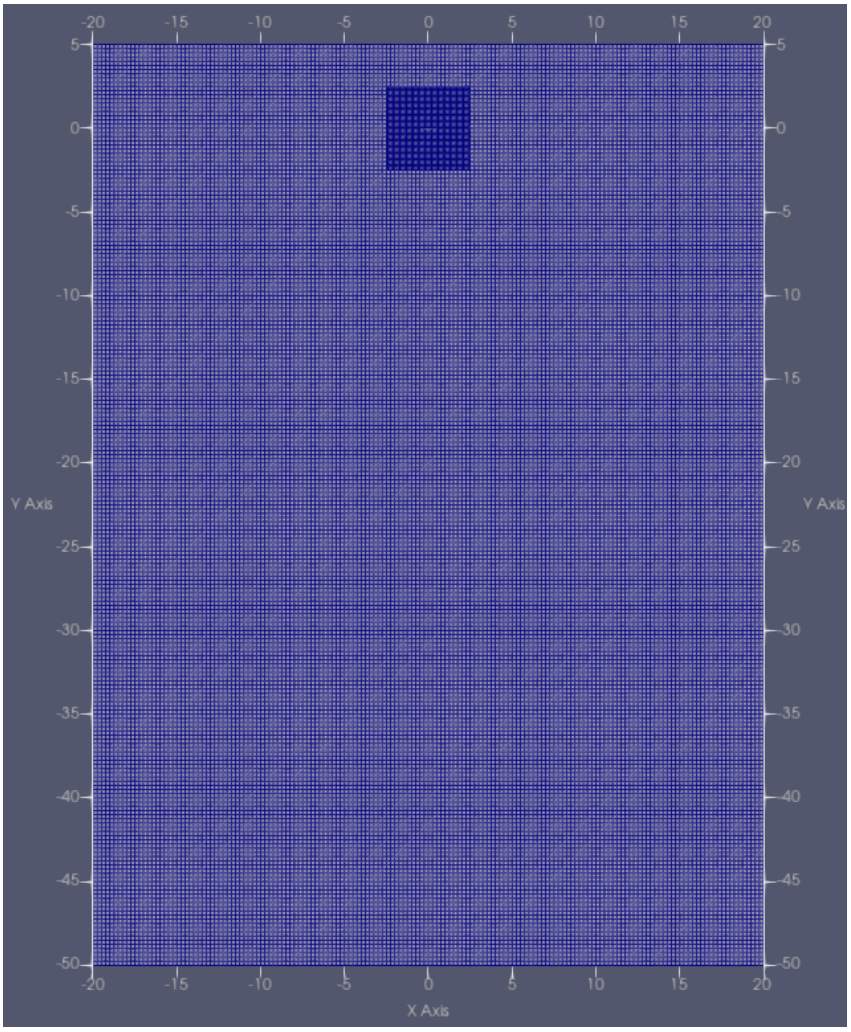

Figure 4: Merged background and overset meshes showing the overlap and hole-cut regions used for interpolation between stationary and moving grids.

Table 2: Computational domain and mesh parameters

Parameter	Value
Background domain dimensions	$40L \times 55L$
Background mesh cell size	$\Delta x = \Delta y = 0.25$
Overset mesh extent	$5L \times 5L$
Overset mesh cell size	$\Delta x = \Delta y = 0.1$
Mesh type	Structured, two-dimensional

The background domain dimensions are selected to minimize the influence of far-field boundaries on the descent dynamics and wake development of the freely falling plate. In particular, the extended vertical extent allows long transients and asymptotic oscillatory behavior to be captured without interaction with the lower boundary. The overset mesh provides local refinement around the plate, enabling accurate resolution of near-body velocity gradients and unsteady

vortex shedding while maintaining a coarser background grid for computational efficiency.

4.3 Boundary Patch Configuration

The overset mesh framework requires consistent patch definitions for both the background and overset meshes. The patches used in the present study are summarized below.

Table 3: Background mesh patch definitions

Patch Name	Patch Type	Physical Role
`oversetPatch`	overset	Interpolation with overset mesh
`left`	patch	Far-field boundary
`right`	patch	Far-field boundary
`up`	patch	Far-field boundary
`down`	patch	Far-field boundary
`frontAndBack`	empty	Enforces two-dimensional flow

Table 4: Overset mesh patch definitions

Patch Name	Patch Type	Physical Role
`oversetPatch`	overset	Interpolation with background mesh
`Flatplate`	wall	Rigid body surface
`frontAndBack`	empty	Enforces two-dimensional flow

4.4 Initial and Boundary Conditions

The flow field is initialized at rest throughout the computational domain, and gravity is applied in the negative vertical direction to drive the free-fall motion. No initial translational or rotational velocity is prescribed for the rigid body.

Boundary conditions are specified separately for the velocity and pressure fields and are applied consistently across background and overset meshes.

Table 5: Velocity boundary conditions

Patch	Patch Type	Velocity Boundary Condition
`Flatplate`	wall	`movingWallVelocity`
`oversetPatch`	overset	`overset`
`left`	far-field	`zeroGradient`
`right`	far-field	`zeroGradient`
`up`	far-field	`zeroGradient`
`down`	far-field	`zeroGradient`
`frontAndBack`	empty	`empty`

The rigid body surface is treated as a no-slip moving wall, with the wall velocity determined by the instantaneous rigid body motion. Overset interface patches use the `overset` boundary condition to enable interpolation between overlapping meshes.

Table 6: Pressure boundary conditions

Patch	Patch Type	Pressure Boundary Condition
`Flatplate`	wall	`zeroGradient`
`oversetPatch`	overset	`overset`
`left`	far-field	`fixedValue` (reference pressure)
`right`	far-field	`fixedValue` (reference pressure)
`up`	far-field	`fixedValue` (reference pressure)
`down`	far-field	`fixedValue` (reference pressure)
`frontAndBack`	empty	`empty`

A uniform reference pressure is imposed at the far-field boundaries to provide a pressure datum, while zero-gradient conditions are applied on the rigid body surface. Overset interfaces exchange pressure information through interpolation during the solution process.

4.5 Solver and Numerical Setup

All simulations are performed using the `overPimpleDyMFoam` solver, which supports transient incompressible flow with overset meshes and dynamic rigid-body motion. Time advancement is controlled using an adaptive time-stepping strategy based on the Courant number to ensure numerical stability during large-amplitude body motion.

Table 7: Solver and time-stepping parameters

Parameter	Setting
Flow solver	`overPimpleDyMFoam`
Pressure–velocity coupling	PIMPLE algorithm
Rigid body solver	`sixDoFRigidBodyMotion`
Initial time step	$\Delta t = 0.001$
Time-step control	Adaptive (`adjustTimeStep`)
Maximum Courant number	$\mathrm{Co}_{\max} = 0.5$
Maximum allowed time step	$\Delta t_{\max} = 0.1$
Turbulence model	Disabled (laminar flow)

All cases are executed in serial using automated `Allrun` scripts to ensure reproducibility.

4.6 Discretization Schemes

The governing equations are discretized using the finite-volume method on structured meshes. Temporal and spatial discretization schemes employed in the present simulations are summarized in Table 8. The selected schemes provide numerical stability for large rigid-body motions and overset mesh interpolation while maintaining reasonable accuracy.

Table 8: Summary of discretization schemes used in the simulations

Category	Term	Discretization scheme
Time discretization	$\partial/\partial t$	`Euler` (implicit)
Gradient schemes	$\nabla(\cdot)$	`cellLimited Gauss linear 1`
Convective terms	$\nabla \cdot (\mathbf{uu})$	`Gauss linearUpwind default`
Diffusive terms	$\nabla^2(\cdot)$	`Gauss linear limited 1`
Interpolation	Cell-to-face	`linear`
Surface-normal gradients	$\nabla_n(\cdot)$	`limited 1`

Overset mesh interpolation is handled separately from the standard spatial discretization. An inverse-distance-weighted interpolation method is employed to exchange solution information across overlapping mesh regions. The overset interpolation parameters used in the present study are listed in Table 9.

Table 9: Overset mesh interpolation parameters

Parameter	Setting
Interpolation method	`inverseDistance`
Hole layers	8
Interpolation layers	4
Search structure	Automatic (voxel-based)

This discretization strategy ensures stable and bounded solutions in the presence of strong advection, mesh overlap, and large-amplitude rigid-body motion.

5 Results and Discussion

This section presents results from two-dimensional numerical simulations of a freely falling flat plate using an overset mesh framework. The plate undergoes coupled translational motion in the x–y plane and rotation about the out-of-plane axis. All results discussed here correspond to the boundary-independent phase of motion, prior to interaction with the computational domain limits.

Simulations are carried out for density ratios ranging from $\rho^* = 8.5$ to 100. Unless stated otherwise, cases up to $\rho^* = 60$ are initialized with an initial angle of attack of $5°$. Additional simulations at $\rho^* = 100$ are performed to examine the influence of the initial angle of attack and computational domain length. The discussion is organized by increasing density ratio, highlighting changes in descent dynamics, angular motion, and transient behavior. Since the plate length is set to $L = 1$ m in all simulations, distances reported in physical units are numerically equivalent to their nondimensional values based on L.

5.1 Descent Dynamics Across Density Ratios

Very low density ratio: steady descent ($\rho^* = 8.5$)

At the lowest density ratio investigated, $\rho^* = 8.5$, the plate exhibits a brief lateral deviation induced by the imposed initial angle of attack, followed by rapid decay of angular motion. No sustained oscillations develop, and the plate aligns with the direction of gravity, descending nearly vertically with a constant descent rate. This indicates that the steady falling state is stable at this density ratio and that flutter does not occur. Such behavior is consistent with previous experimental and numerical studies, which report that at sufficiently low inertia the steady descent state remains stable and angular perturbations decay rather than develop into sustained oscillatory motion [1, 2].

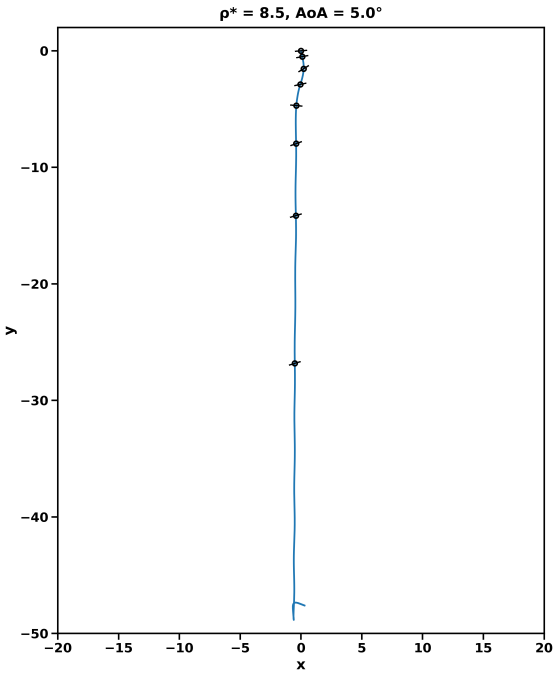

Figure 5: Trajectory of the flat plate for $\rho^* = 8.5$ and initial angle of attack $5°$, showing rapid damping of angular motion and steady descent.

Low density ratios: flutter onset and transition to tumbling ($\rho^* = 9$–15)

For density ratios slightly above $\rho^* = 8.5$, the steady descent state loses stability and sustained angular oscillations develop. The plate initially exhibits fluttering motion characterized by oscillatory changes in orientation with periodic reversal of rotation direction. In this density-ratio range, the vertical displacement histories exhibit two distinct slopes, indicating the presence of two dynamically different phases during the fall.

During the early phase, the plate descends with a lower mean vertical velocity while undergoing flutter. As the descent progresses, the oscillation amplitude grows, and the fluttering motion becomes unstable, leading to a qualitative change in the coupled translational–rotational dynamics. This change is marked by the emergence of continuous rotation without reversal and a corresponding increase in the mean descent velocity. The distance required for the onset of this transition increases with the density ratio within this range.

Following the classification used in previous studies, this behavior is identified as a transition from fluttering motion to tumbling, characterized by continuous autorotational motion.

The appearance of two distinct slopes in the vertical displacement histories is a characteristic signature of this flutter–tumbling transition [1, 2].

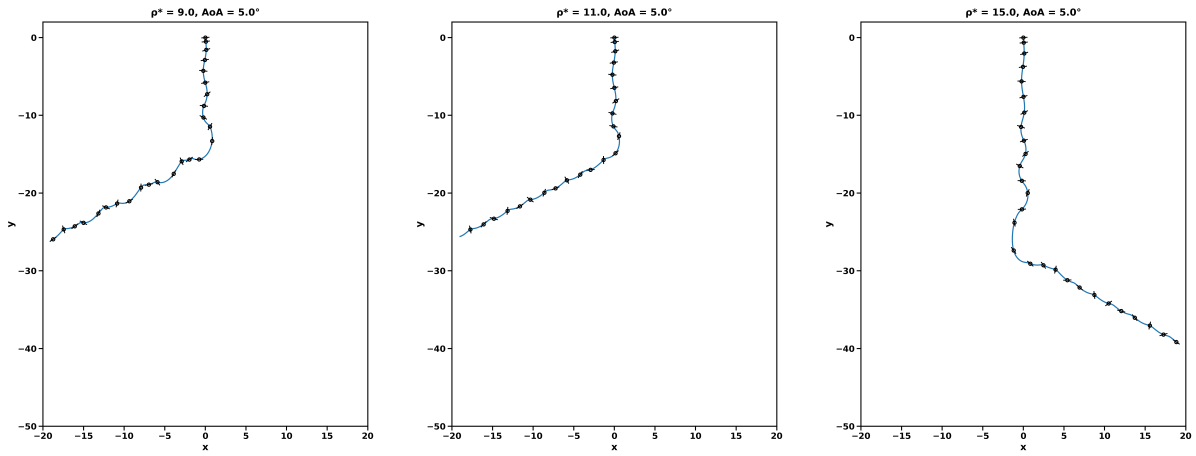

(a) $\rho^* = 9,\ \text{AoA} = 5^\circ$ (b) $\rho^* = 11,\ \text{AoA} = 5^\circ$ (c) $\rho^* = 15,\ \text{AoA} = 5^\circ$

Figure 6: Trajectories illustrating flutter onset, growth of oscillation amplitude, and transition to tumbling (autorotation) for increasing density ratio.

Intermediate density ratio: stable flutter ($\rho^* \approx 30$)

At intermediate density ratios, exemplified by $\rho^* \approx 30$, the plate exhibits sustained oscillatory motion throughout the descent. The angular motion remains bounded, with repeated reversals of rotation direction, and no continuous rotation about the center of mass is observed. In contrast to the low-density cases, the vertical displacement history shows a single, nearly constant slope, indicating that the mean descent velocity is established early and remains unchanged.

In the baseline computational domain, approximately 8–10 oscillation cycles are observed over the simulated fall distance. A slow lateral drift accompanies the oscillatory motion, but no abrupt changes in trajectory occur. The oscillations become regular after a relatively short transient, and the motion settles into a repeatable pattern after approximately 25–30 m of descent. This behavior corresponds to a stable flutter regime, in which bounded oscillations persist without evolving into steady descent or tumbling, as reported in earlier studies of freely falling plates [2].

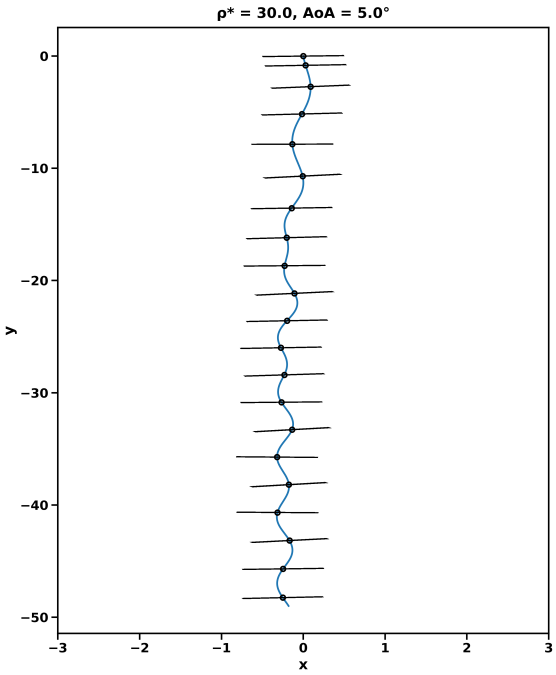

Figure 7: Trajectory for $\rho^* \approx 30$ showing bounded oscillations, single-slope vertical descent, and stable flutter.

High density ratios: strongly inertial stable flutter ($\rho^* = 60$–100)

For higher density ratios, the qualitative nature of the motion remains oscillatory, but the transient dynamics become significantly longer. At $\rho^* \approx 60$, the plate exhibits bounded oscillations with periodic reversal of rotation direction and very slow lateral drift. The number of oscillation cycles reduces to approximately 5–6 over a comparable fall distance, reflecting the increased rotational inertia of the plate. The motion converges to a regular oscillatory pattern only after approximately 75–80 m of descent.

At $\rho^* = 100$ and an initial angle of attack of $5°$, the oscillation amplitude is small, and the transient persists over a much larger fall distance. Although oscillations may appear to decay in shorter computational domains, extended simulations reveal convergence to a bounded, repeatable oscillatory state. As in the $\rho^* \approx 30$ and 60 cases, the vertical displacement history exhibits a single slope, indicating that the mean descent velocity is established early, and that no regime transition occurs during the fall.

The reduction in oscillation frequency with increasing density ratio is consistent with the increase in rotational inertia, which reduces angular acceleration and leads to longer oscillation wavelengths in physical space. Similar trends have been reported for freely falling plates and disks in both numerical and experimental studies [3].

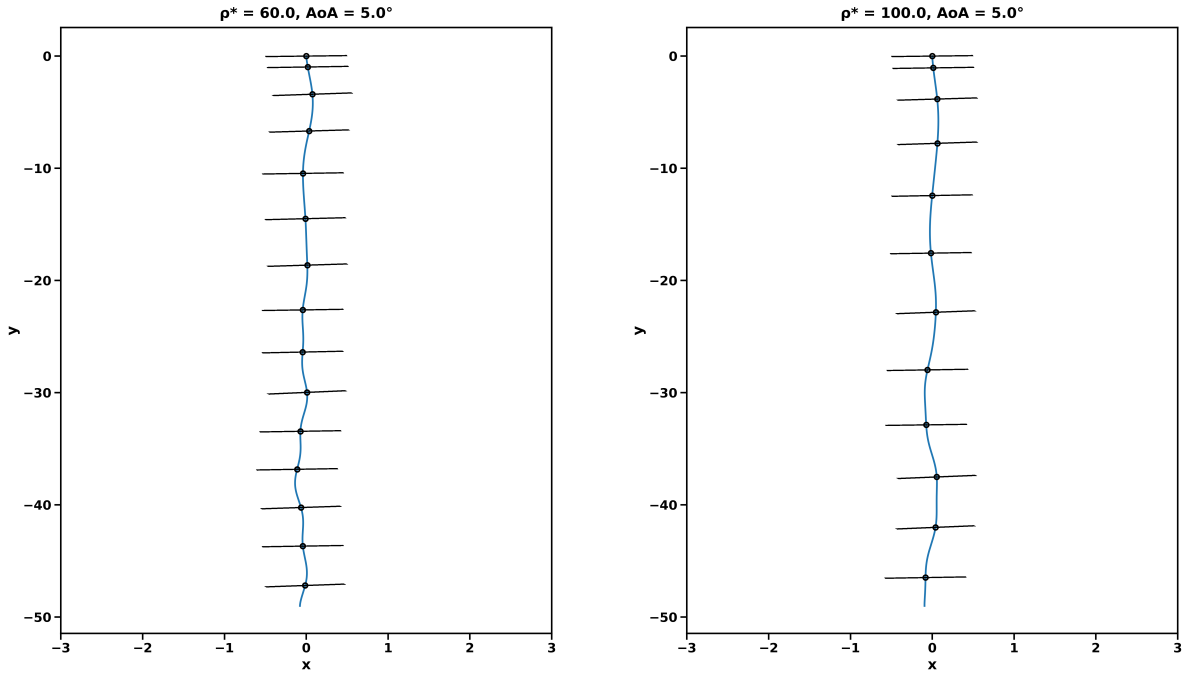

(a) $\rho^* = 60,\ \text{AoA} = 5^\circ$ (b) $\rho^* = 100,\ \text{AoA} = 5^\circ$

Figure 8: Comparison of trajectories illustrating reduced oscillation frequency and prolonged transient behavior at high density ratios.

The sequence of observed descent regimes and their dependence on the density ratio are in qualitative agreement with earlier experimental and numerical studies on freely falling plates, including the onset of flutter, the flutter–tumbling transition, and the persistence of stable flutter at higher inertia [1, 2, 3].

5.2 Effect of Initial Angle of Attack at $\rho^* = 100$

Additional simulations at $\rho^* = 100$ are performed with initial angles of attack of 5°, 30°, 60°, -30°, and -60°. Increasing the initial angle of attack leads to larger oscillation amplitudes during the transient phase, while reversing the sign of the angle produces mirrored trajectories, with the direction of lateral motion reversed accordingly. These observations are consistent with the symmetry of the governing equations indicate that the initial angle of attack acts as a perturbation amplitude rather than a selector of the long-time dynamical regime [3].

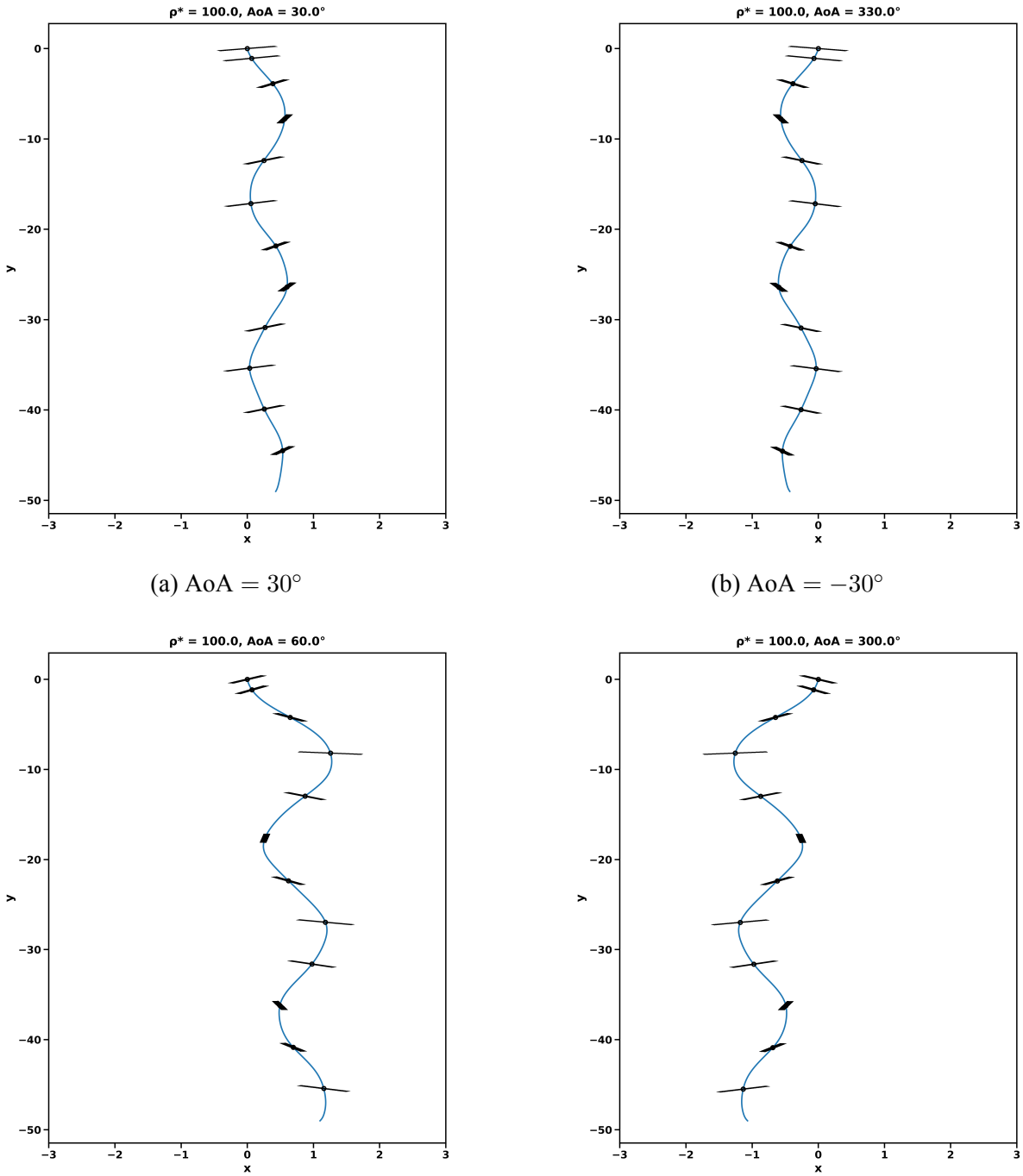

(a) AoA $= 30°$

(b) AoA $= -30°$

(c) AoA $= 60°$

(d) AoA $= -60°$

Figure 9: Effect of initial angle of attack on descent trajectories for $\rho^* = 100$. Increasing the magnitude of the angle enhances transient oscillation amplitude, while opposite signs lead to mirrored descent paths.

5.3 Effect of Computational Domain Length

At high density ratios, the long transient duration necessitates extended computational domains to accurately capture the asymptotic behavior. For $\rho^* = 100$ and an initial angle of attack of $60°$, simulations performed in an extended vertical domain demonstrate that the oscillatory motion

does not decay to steady descent. Instead, after a prolonged transient, the system converges to a stable, periodic oscillation with constant amplitude and frequency. This behavior is characteristic of a limit-cycle oscillation of the coupled translational–rotational system, as described in previous studies of stable flutter regimes [2].

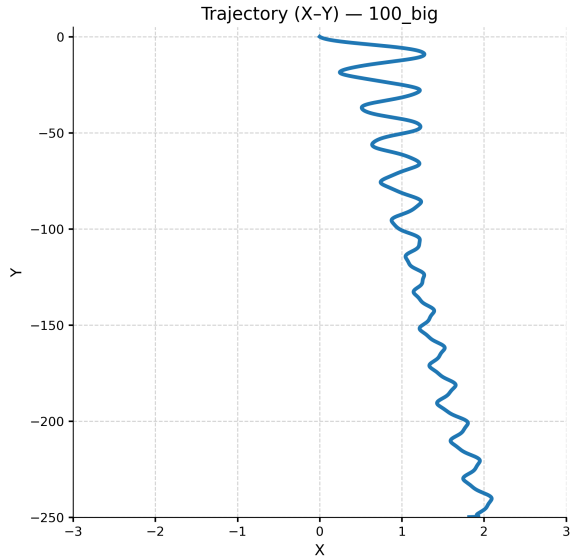

Figure 10: Extended-domain simulation for $\rho^* = 100$ and initial angle of attack $60°$, demonstrating convergence to a stable limit-cycle oscillation.

5.4 Summary of Observed Regimes

Table 10: Summary of observed descent regimes across density ratios

Density ratio (ρ^*)	Observed behavior	Identified regime
8.5	Damped angular motion	Steady descent
9–15	Flutter with slope change in $y(t)$	Flutter $\rightarrow$ tumbling
$\sim$30	Bounded oscillations, short transient	Stable flutter
60–100	Bounded oscillations, long transient	Strongly inertial stable flutter

Table 11: Approximate transient lengths for selected density ratios

Density ratio (ρ^*)	Transient length (m)	Oscillation count
$\sim$30	25–30	8–10
$\sim$60	75–80	5–6
100	$\sim$150	Few, long-wavelength

6 Conclusion

This work examined the use of overset meshes in `OpenFOAM` for simulating freely falling rigid bodies undergoing large translational and rotational motion. A two-dimensional, laminar formulation was coupled with a six-degree-of-freedom rigid body solver, allowing the motion to be resolved without mesh deformation while maintaining stable interaction between the flow and the body.

The free fall of a flat plate with finite thickness was studied over density ratios ranging from $\rho^* = 8.5$ to 100. With increasing density ratio, the descent behavior evolved from steady vertical motion to sustained flutter and, at higher inertia, to long-duration oscillatory motion with extended transients. Increasing rotational inertia delayed convergence to asymptotic behavior and reduced oscillation frequency, leading to longer physical wavelengths in the descent trajectory.

Extended-domain simulations were essential for correctly interpreting the high-inertia cases. Motions that appeared to decay in shorter computational domains were shown to converge to bounded, repeatable oscillations when sufficient fall distance was provided. This indicates that the long-time response corresponds to a stable limit-cycle behavior of the coupled translational–rotational system rather than true damping.

While the present work is restricted to two-dimensional, laminar flow and focuses on qualitative motion characteristics, the numerical framework can be naturally extended in several directions. Possible extensions include three-dimensional simulations to examine spanwise effects and finite aspect ratio, detailed analysis of wake structures and vortex dynamics, and quantitative evaluation of aerodynamic forces and moments. The overset mesh approach adopted here also provides a suitable basis for studying more complex fluid–structure interaction problems involving flexible bodies or controlled motion.

References

[1] U. Pesavento and Z. J. Wang. Falling paper: Navier–stokes solutions, model of fluid forces, and center of mass elevation. *Physical Review Letters*, 93(14):144501, 2004.

[2] A. Andersen, U. Pesavento, and Z. J. Wang. Unsteady aerodynamics of fluttering and tumbling plates. *Journal of Fluid Mechanics*, 541:65–90, 2005.

[3] T. C. W. Lau, K. T. Tse, and K. C. S. Kwok. Fluttering and tumbling of rectangular plates in free fall. *Journal of Fluids and Structures*, 80:165–178, 2018.

[4] N. Rana and S. Mittal. Flutter and tumbling dynamics of freely falling plates. *Physics of Fluids*, 32(4):043601, 2020.

[5] D. Sohn and J. Zhang. Inertial effects on the free fall of plates: A vortex-sheet model. *Journal of Fluid Mechanics*, 982:A12, 2024.